Using Side Reactions for Extra Capacitive Energy Storage Based on Spin Regulated MnO_2

Yi Wan, Yujie Xu, Bin Wang, Tong Cao, Daliang Zhang, Qiang Li, Alistair J. Fielding, Mingbo Wu, Han Hu

ABSTRACT

Pseudocapacitive materials in neutral aqueous electrolytes are promising for large-scale energy storage but are hindered by parasitic reactions like the oxygen evolution reaction (OER). This work demonstrates that spin-regulated MnO_2 can redirect such side reactions toward capacitive storage by modulating the rate-determining step. Theoretical analysis indicates that MnO_2 with unpaired e_g electrons facilitates water dissociation, the initial OER step, while stabilizing intermediates *OH on active sites to prevent the subsequent gas evolution. This channels the charges associated with water dissociation into additional capacitive charge storage. By engineering Mn and O vacancies in MnO_2 to delocalize e_g electrons, a 53% capacitance increase and markedly enhanced rate capability are achieved. In situ characterizations, especially electron paramagnetic resonance, confirm that water dissociation is driven by a double exchange interaction along Mn^{3+} (e_g^1)–O^{2-}–Mn^{4+} (t_{2g}^3), consistent with theoretical simulations. This work offers a practical approach to enhance MnO_2-based pseudocapacitors and deepens the understanding of their charge storage mechanisms.

1 Introduction

Potential-dependent adsorption of water molecules on the surface of electrode materials represents one of the fundamental processes for modern electrochemistry [1-3]. Gaining a profound understanding of this phenomenon is crucial for the application of innovative electrochemical technologies. Such understanding has been instrumental in the development of electrocatalysts for water splitting in both acidic and alkaline electrolytes, facilitating the widespread deployment of green hydrogen production for a sustainable future [4, 5]. Beyond its role in green hydrogen generation, the interaction of water molecules with electrode materials is also pivotal for aqueous supercapacitors, an emerging technology for large-scale energy storage. Within the operational potential range of these materials, water molecules in various configurations engage with the electrodes, significantly impacting the capacitive performance of the materials [6, 7]. Recent studies have meticulously examined the influences of adsorbed water on pseudocapacitive materials, such as MnO_2, MXenes, etc., in neutral electrolytes [8-10]. These investigations have yielded intriguing findings that have substantially expanded our knowledge of pseudocapacitive mechanisms. As a result, the performance of pseudocapacitive materials has seen continuous enhancement.

The interaction between water molecules and pseudocapacitive materials, for example MnO_2, in neutral electrolytes at the potential limits has long been overlooked. This oversight is primarily due to the high risk associated with side reactions of water decomposition to produce gas, such as the oxygen evolution reaction (OER) (Figure S1) at the upper potential limit [11]. The gas evolution adversely affects the stability of electrode materials, electrolytes,

and the overall performance of the devices. Consequently, strategies to mitigate this risk, such as passivating the electrode surface or narrowing the operating potential, are commonly employed in practical applications [12]. The OER typically entails the transfer of multiple electrons, with gas generation only at/after the last electron transfer [11]. As a result, the energy expended on electron transfer prior to the step of gas evolution could potentially be redirected to enhance the stored energy for the MnO_2.

The crux of harnessing the energy from the side reactions lies in modulating the rate-determining steps. For instance, significantly lowering the free energy of water dissolution in neutral electrolytes but restricting the subsequent charge transfer could partially harvest the energy without the risk of gas evolution [13]. The aforementioned process generally offers a finite increase in current density and generates transient intermediate species, in contrast to the large polarized current and stably evolved gases for electrocatalytic processes. The subtle responses, however, yield weak structural and procedural signals, making the acquisition of detectable signals for this process quite challenging. As a result, the ideal structural features that facilitate gas-absence side reactions at the potential limits remain obscure. Recently, the spin evolution of charge transfer and finely regulated electrode materials have been investigated using electron paramagnetic resonance (EPR) spectroscopy, providing pivotal insights for mechanism elucidation and structural optimization of critical materials [14-18]. In contrast to other characterization techniques, the detection of electron spin with EPR offers exceptional sensitivity [19]. Therefore, employing EPR to decipher the electrochemical processes under mild conditions and subtle structural variation is set to yield a wealth of information, illuminating the pathways to enhance energy storage capability.

In this work, we propose the modulation of the spin state of MnO_2 as a means to leverage water dissociation, the inaugural step of the OER, for augmenting capacitive energy storage. The optimal spin configuration for MnO_2-based materials tailored for this purpose was hypothesized and substantiated through density functional theory (DFT) calculations, where the double exchange interaction along Mn^{3+} (e_g^1)–O^{2-}–Mn^{4+} (t_{2g}^3) plays a key role. Due to this interaction, the sluggish charge transfer for water dissociation is accelerated while the energy barrier for further charge transfers is boosted on MnO_2 in neutral electrolytes. Based on this inspiration, such a structure was constructed by dual vacancy regulation that contributes to a 53% enhancement in capacitive energy storage. In situ characterization, especially EPR, was used to monitor intermediate species arising from water dissolution, providing direct evidence of the dissociative intermediates as well as the double exchange interaction that underpins the observed enhancement in energy storage. These findings robustly establish the influence of spin structure on pseudocapacitive energy storage of MnO_2. An additional intriguing observation is that the spin-regulated MnO_2 exhibits improved rate performance, underscoring the significance of spin state in dictating electrochemical behavior. The outcomes of this study not only elucidate the critical role of spin state in optimizing the performance of emerging electrode materials but also deepen our understanding of the fundamental electrochemical processes. By demonstrating the interplay between spin

structure and pseudocapacitive materials, this work paves the way for the design of advanced materials with tailored spin structures for high-efficiency energy storage applications.

2 Results and Discussion

2.1 Theoretical Investigation of Spin Evolution and Catalytic Performance

To identify suitable structures for extracting energy from side reactions, a typical pseudocapacitive material, MnO_2, with different vacancy-deficient structures was modeled (Figures **1A,D** and **S2–S4**). The projected density of states (PDOS) calculation of these structures reveals that the MnO_2 model with both Mn and O vacancies (DV-MnO_2) exhibits the highest DOS at the occupied states below the Fermi level (Figure **1E**) compared to MnO_2 without defects (labeled as MnO_2) (Figure **1B**) and MnO_2 with oxygen vacancies (OV-MnO_2) (Figure **S3B**). Consequently, more unpaired spin-up e_g electrons at the d_z^2 orbital, are observed for DV-MnO_2 (Figure **1C,F**; Figure **S3C**), suggesting a larger extent of electron delocalization, as further confirmed by the electron localization function (inset of Figures **1C,F** and **S3C**) [**20**, **21**].

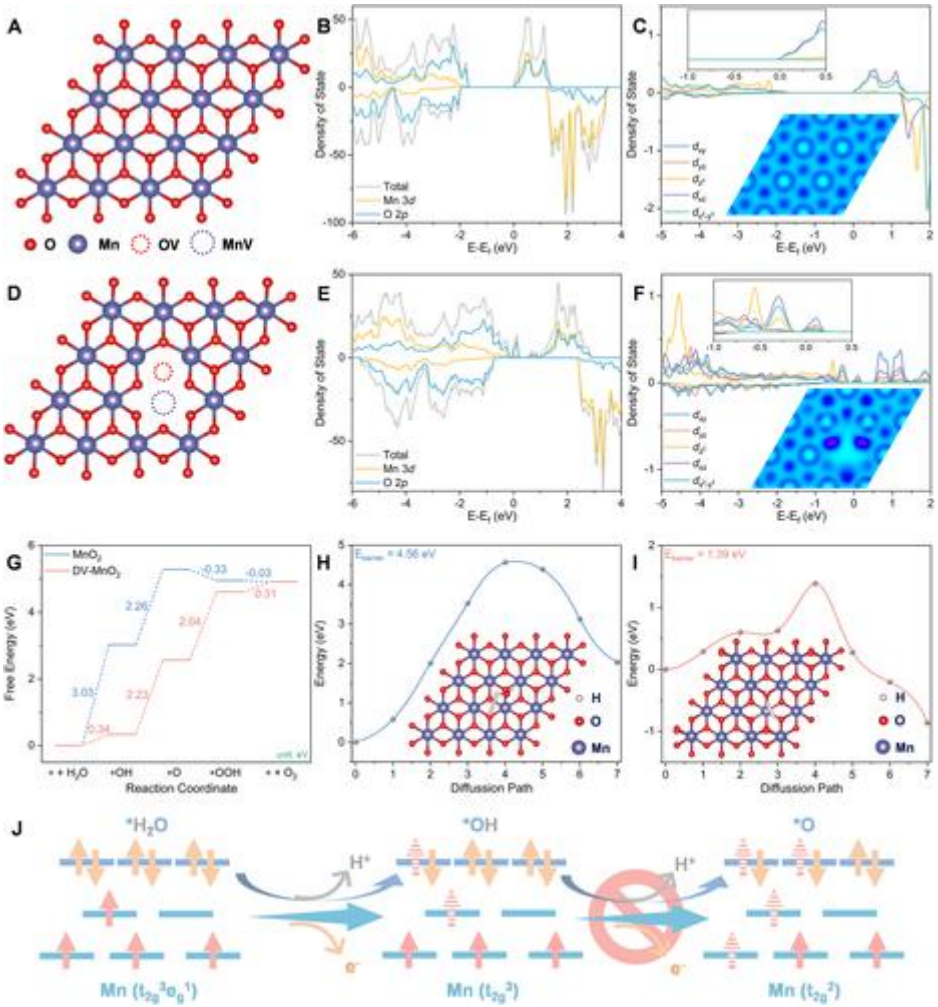

FIGURE 1

Open in figure viewerPowerPoint

First-principles study. (A) Structural model, (B) PDOS, and (C) Mn-PDOS of MnO_2. (D) Structural model, (E) PDOS, and (F) Mn-PDOS of DV-MnO_2. (G) The free energy diagram of OER on MnO_2 and DV-MnO_2. Energy barrier and pathways of water dissociation on (H) MnO_2 and (I) DV-MnO_2. (J) Illustrated scheme of the reversible water dissociation driven by DV-MnO_2.

The impact of these structures on OER was compared in Figures **1G** and **S5**. A noteworthy discovery is that the free energy for the initial step of OER, namely the water dissociation ($H_2O + * \leftrightarrow *OH + H^+ + e^-$), can be regulated in a wide range, indicating that the transferred charges at this stage offer high potential for additional energy storage. Although the OV-MnO_2 is the most active structure for water dissociation, the strongly adsorbed *OH species (−0.55 eV) (Figure **S3D**) necessitates an extremely negative potential for desorption (−1.2158 V vs. SCE), which precludes the reversibility of this step. Triggering the water dissociation on MnO_2 demands a high energy (Figure **1G**), but the subsequent steps toward the gas evolution would be facilitated, which also needs to be excluded as a suitable candidate for harnessing the energy from side reactions. As for the DV-MnO_2 (Figure **1G**), a moderate free energy for water dissociation is observed, thus enabling a high reversibility of this step. From a kinetics perspective, the energy barrier for this step on MnO_2 and DV-MnO_2 is 4.56 (Figure **1H**) and 1.39 eV (Figure **1I**), respectively, corresponding to applied potentials of 3.89 and 0.72 V versus SCE. In addition, the free energy for the subsequent electron transfer is much larger than that of the first step, offering a high possibility of storing energy from water dissociation. For reliable utilization of the structure for energy storage, a highly stable structure is strongly needed. The ab initio molecular dynamics simulations demonstrate excellent stability of the defect-rich DV-MnO_2, with no bond breaking or geometry reconstruction for a long duration (Figure **S6**), as well as the phonon dispersion curves (Figure **S7**). As a result, DV-MnO_2 can be regarded as a promising structure to harvest energy from the water-involved side reaction. Based on the elaborated theoretical investigation, a possible hypothesis for this purpose can be concluded as follow (Figure **1J**): (i) the highly delocalized e_g electron from the Mn sites interacts with the p_z orbital of O at H_2O (Figures **S8** and **S9**), triggering the water dissociation at a desired potential (0.72 V vs. SCE); (ii) the as-generated *OH interacts with t_{2g} orbitals of Mn which results in a highly localized electron distribution to prohibit the further dehydrogenation of *OH to *O (Figure **S10**) [**22**-**25**].

2.2 Synthesis and Structural Characterizations

Inspired by the aforementioned theoretical calculation, a certain amount of O and Mn in the hydrothermal MnO_2 were extracted by Li-ethylenediamine (LEDA) to produce DV-MnO_2 (Figure **S11A**). Specifically, Li in the LEDA, as a strong electron donor, attacks the metal sites to generate OVs, while the neighboring Mn is simultaneously extracted by the chelating effect of EDA to form Mn vacancies (MnVs) (Figure **S11B**) [**26**-**28**]. Scanning electron microscopy (SEM) images (Figure **S12**) reveal that the overall structure of the DV-MnO_2 is well maintained. Nitrogen adsorption-desorption isotherms indicate that the two materials have similar specific surface areas (12.1 and 17.6 $m^2 g^{-1}$) and pore size distributions (Figure **S13**). X-ray diffraction (XRD) patterns in Figure **2A** demonstrate that all diffraction peaks in the as-synthesized MnO_2 and DV-MnO_2 can be well indexed to the birnessite-type MnO_2 (JCPDS No.

52–0556). The vacancies, however, disrupt the local structure, resulting in decreased diffraction intensity. High-resolution transmission electron microscopy (HRTEM) in Figure 2B and Figure S14 verifies a layered structure with a spacing of 0.66 nm for both MnO_2 and DV-MnO_2, but a disordered distribution of atoms for DV-MnO_2 (Figure S12C,G). The variation of valence state was then investigated by X-ray photoelectron spectroscopy (XPS), where DV-MnO_2 shows a lower Mn valence state (Figure 2C). Specifically, the average oxidation state of DV-MnO_2 is 3.49 compared to 3.72 for the as-synthesized counterpart (Figure S15) [29]. Moreover, the reduced content of lattice oxygen ($O_{lattice}$) and increased OVs in DV-MnO_2 are reflected in the O 1*s* spectra (Figure 2D), agreeing well with the variation of Mn spectra [14]. The higher content of OVs in DV-MnO_2 incurs a distinct signal at g = 2.0036 in the EPR spectra due to the unpaired electron from OVs (Figure S16) [30]. The structural evolution induced by LEDA was further disclosed by X-ray absorption spectroscopy (XAS). As shown in Figure 2E, the absorption edge of the Mn *K-edge* shows a shift to lower energy for DV-MnO_2 (inset in Figure 2E), indicating a reduction in the Mn valence state. The *R*-space of the Mn *K*-edge $k^3\chi(k)$ spectra in Figure 2F, fitted from the extended X-ray absorption fine structure (Figure S17), reveals a simultaneously decreased coordination number of Mn–O and Mn–Mn_{edge} for DV-MnO_2, suggesting the existence of MnVs and OVs (Table S1) [31]. The evolved coordination structure was further confirmed by aberration-corrected scanning transmission electron microscopy (AC-STEM). The regular triangular lattice of MnO_2 (Figure S18) could still be maintained but with obvious local defects after LEDA treatment because of the loss of Mn (Figure 2G–I), coinciding well with the aforementioned characterization.

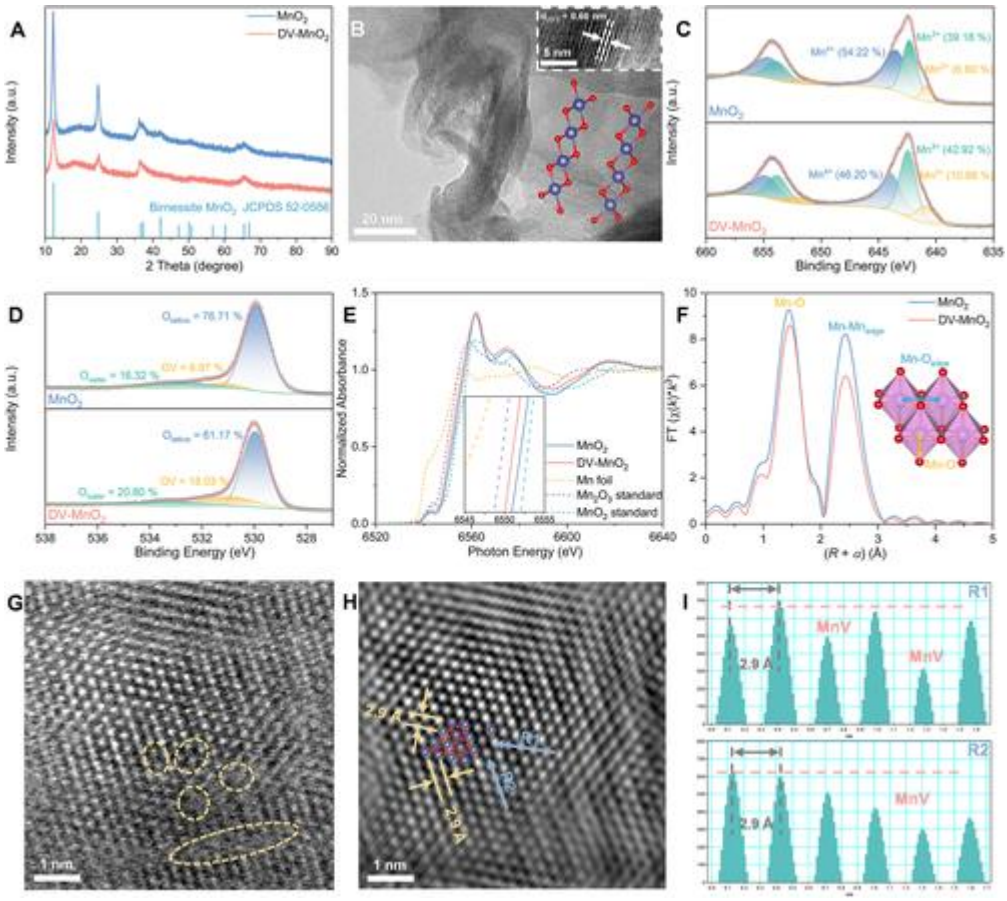

FIGURE 2

Open in figure viewerPowerPoint

Characterization of MnO_2-based electrodes. (A) XRD patterns of the MnO_2 and DV-MnO_2. (B) HRTEM image of DV-MnO_2. (C) Mn 2*p* and (D) O 1*s* XPS spectra of MnO_2 and DV-MnO_2. (E) Mn *K*-edge X-ray absorption near-edge structure spectra of MnO_2, DV-MnO_2, Mn foil, MnO_2 standard, and Mn_2O_3 standard. (F) Radial distribution functions of MnO_2 and DV-MnO_2. (G) AC-STEM image of DV-MnO_2 along the [001] zone axis. (H) The filtered image of (G), and (I) the corresponding normalized intensity variation of the column along the arrows in (H).

To understand the impact of vacancies on electronic structure, soft-XAS was conducted to reveal the occupied state of Mn 3*d* orbitals. The L_3 edge spectra of Mn *L*-edge XAS (Figure **3A**) in total electron yield mode split into two peaks, corresponding to the t_{2g} and e_g energy levels [**32**]. DV-MnO_2 shows enhanced t_{2g} intensity but decreased e_g intensity with respect to MnO_2, suggesting a lower electron density in t_{2g} orbitals but an increased density in e_g orbitals at the ground state [**33**]. Moreover, the weakened intensity and reduced area ratio of two peaks in O *K*-edge XAS spectra of DV-MnO_2 (Figure **3B**) indicate a weakened electronic interaction between Mn–O bonds due to electron delocalization [**34**, **35**]. The bridging oxygen between metal ions with different e_g fillings could contribute to double exchange channels, which facilitate the interaction between delocalized electrons and water molecules for promoted water dissociation [**36**-**38**]. In our case, the detailed electron filling of Mn^{3+} in DV-MnO_2 is revealed by magnetic measurements where an e_g electron is confirmed (Figure **3C,D**), consistent with the soft XAS measurement [**39**]. Moreover, the Mn^{3+} connects with Mn^{4+} through the bridge of O^{2-} in a spatial configuration that is almost 90° (Figure **S19**). Such an electronic and spatial configuration in DV-MnO_2 permits the double exchange interaction as illustrated in Figure **3E** [**24**, **40**], which is capable of facilitating water dissociation. Additionally, DV-MnO_2 exhibits a weaker and broader EPR spectrum compared to MnO_2 (Figure **3F**), due to the strong electron-electron dipolar interaction superimposing on Zeeman's interactions, further confirming the double exchange interaction [**41**-**44**]. The interaction is also confirmed by field-dependent magnetization (Figure **S20**) and magnetic force microscope measurements, because of a higher contribution of ferromagnetism (Figure **S21**) [**24**, **40**].

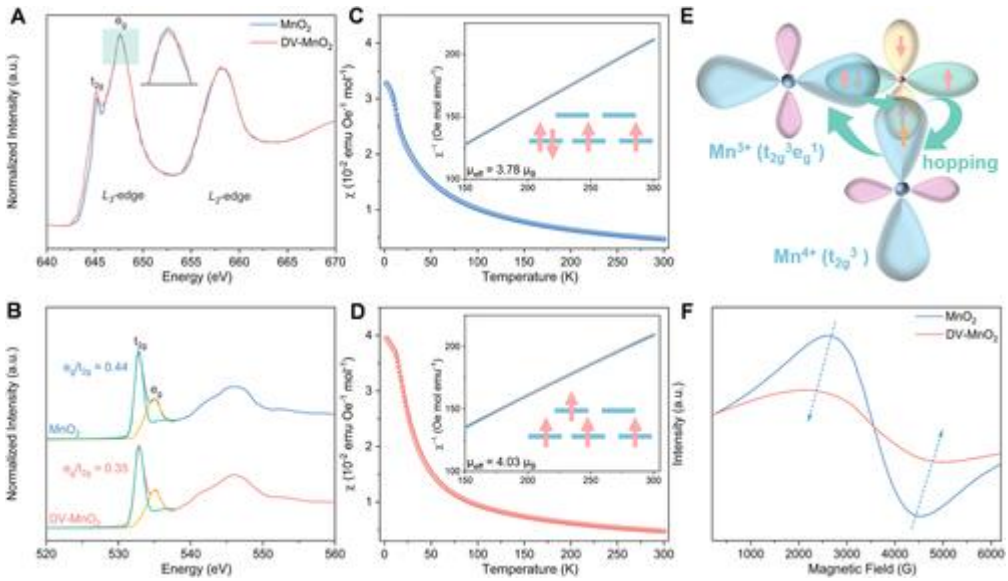

FIGURE 3

[Open in figure viewerPowerPoint]

XAS and magnetic characterization. (A) Mn $L_{2,3}$-edge XAS and (B) O *K*-edge XAS of the MnO_2 and DV-MnO_2. M-T measurements of (C) MnO_2 and (D) DV-MnO_2 (Inset: the obtained occupied state of Mn 3*d* orbitals). (E) Schematic illustration of double exchange interaction via Mn^{3+} (e_g^1)–O^{2-}–Mn^{4+} (t_{2g}^3). (F) EPR spectra of the MnO_2 and DV-MnO_2.

2.3 Electrochemical Performance

To unravel the influence of e_g electrons on pseudocapacitive energy storage, electrochemical measurements were conducted using a three-electrode configuration in a neutral electrolyte. As shown in Figures **4A** and **S22**, both MnO_2-based electrodes exhibit pseudocapacitive behavior characterized by quasi-rectangular cyclic voltammetry (CV) profiles [**45**]. The CV curve of the DV-MnO_2 encloses a larger area compared to that of the MnO_2, indicating a higher pseudocapacitive capacitance. This is further confirmed by the galvanostatic charge–discharge (GCD) measurements, where the specific capacitance increases from 107.2 to 164.4 F g^{-1}, as shown in Figure **4B**. The capacitance increase is further enhanced at high current densities (Figure **4C**), attributed to the acceleration of the charge transfer process by e_g electron (Figure **S23**). Compared to the CV curve of the MnO_2, a severe polarization is observed for the DV-MnO_2 in the potential range of 0.75–0.9 V versus SCE (Figure **4A**). After increasing the amount of lithium metal added, similar electrochemical behavior is maintained; however, the excessively high defect concentration leads to a slight decrease in specific capacitance (Figure **S24**). Generally, polarization at this potential is associated with side reactions, such as OER. However, the presence of a current hump during reverse scan suggests a potentially reversible process. As shown in Figures **S25** and **S26**, the CV curves of carbon paper and carbon cloth as current collectors, as well as bare nickel foam, exhibit similar characteristics, ruling out polarization caused by the current collectors.

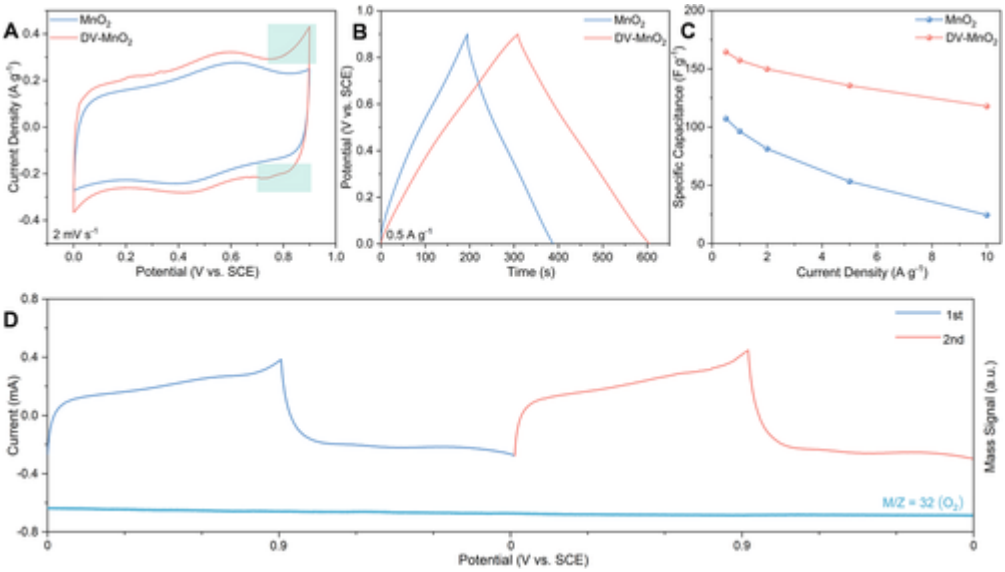

FIGURE 4

[Open in figure viewerPowerPoint]

Electrochemical performance of MnO_2-based electrodes. (A) CV curves of the MnO_2 and DV-MnO_2 electrodes measured at a scan rate of 2 mV s^{-1}. (B) GCD profiles recorded at a current density of 0.5 A g^{-1}. (C) Rate capability of two MnO_2-based electrodes. (D) In situ DEMS of DV-MnO_2 electrode measured at a scan rate of 2 mV s^{-1}.

For the OV-MnO_2 electrode (Figure S27), oxygen vacancies can catalyze the decomposition of water molecules, resulting in a polarization peak at high potentials. However, the peak current density at the high potential gradually decreases, attributed to the irreversible electrochemical reaction caused by the strong adsorption of *OH, while the other potential regions remain largely overlapping (Figure S27B), which is consistent with the DFT calculation results. This poor electrochemical reversibility leads to the inferior electrochemical performance of OV-MnO_2, with a specific capacitance of 127.8 F g^{-1} at a current density of 0.5 A g^{-1}.

The reversibility of the polarization is confirmed by in situ differential electrochemical mass spectroscopy (DEMS). As shown in Figure 4D, the absence of an O_2 evolution signal throughout the entire scan indicates that the polarization may be related to one or two electron transfer steps of OER before gas evolution. To further eliminate the OER and the trace dissolved oxygen, the potential range was extended to 0–1.1 V (vs. SCE). As shown in Figure S28, a pair of reversible polarization peaks appears at high potentials, and no large polarization current arising from the OER is observed. Furthermore, the two-electron transfer side reaction producing hydrogen peroxide was ruled out by iodometric titration, as well as the Gibbs free energy calculation (Figure S29).

2.4 Investigation of Water Dissociation Mechanism

To unravel the actual reactions occurring during anodic polarization, in situ Raman measurements were firstly carried out. As shown in Figure S30, three Raman bands, namely

v_1, v_2, and v_3, were observed for MnO_2-based electrodes, which correspond to symmetric stretching vibration of Mn–O bond in MnO_6 octahedral, Mn–O stretching vibration along chains of the MnO_2 framework, and Mn–O bond vibration between adjacent layers, respectively [46]. During charging (Figure 5A,B), these Raman bands evolve in a similar manner for both electrodes. The enhanced v_1 and v_2 bands suggest the extraction of Na^+ ions and oxidation of Mn^{3+} to Mn^{4+}, respectively, and vice versa during discharging. The v_3 band undergoes a slight blue shift during charging, which is attributed to the Na^+ ion extraction and the intercalation of H_2O [47, 48]. It is worth noting that a weak band at 380 cm^{-1} appears around 0.7 V versus SCE during charging and disappears around 0.45 V versus SCE during discharging (right panel of Figure 5B) for DV-MnO_2. This band is assigned to the Mn–OH vibration band (Figure S31) [49]. The periodic appearance of Mn–OH may suggest the reversible generation of *OH through one-electron transfer water dissociation, which is catalyzed by delocalized e_g electrons due to double exchange interaction.

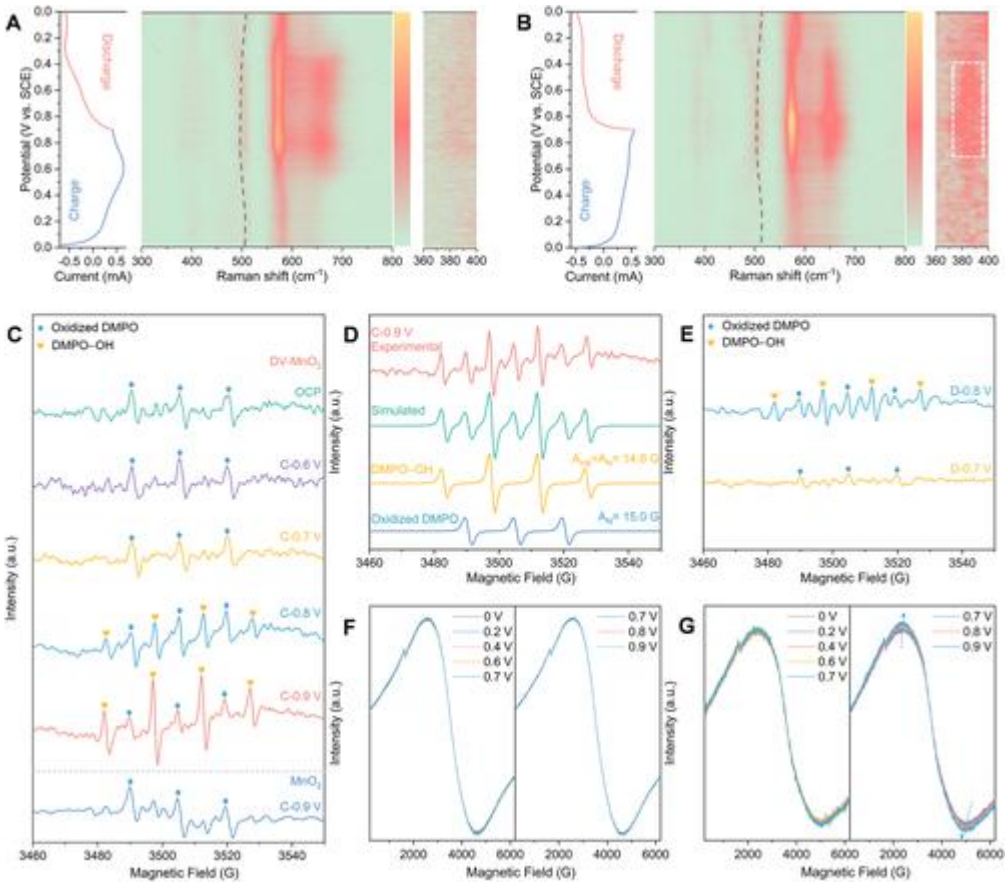

FIGURE 5

[Open in figure viewerPowerPoint]

In situ characterization for intermediates. In situ Raman spectra of (A) MnO_2 and (B) DV-MnO_2 at a scan rate of 2 mV s^{-1}. (C) In situ EPR spectra for capturing intermediate species by DMPO at different potentials. (D) Comparison of the experimental EPR signal with simulated signals. (E) Ex situ EPR spectra of the capturing intermediate species during the discharge process. In situ EPR spectra of (F) the MnO_2 and (G) the DV-MnO_2 at different potentials in pure water.

A homemade in situ cell (Figure S32) was constructed for an EPR test to identify the intermediates. An Ag wire served as the reference electrode (Figure S33). The trapping agent of 5, 5-dimethyl-1-pyrroline-1-oxide (DMPO) was introduced to capture the intermediates. As shown in Figure 5C, three major peaks are observed for DV-MnO_2 at the open-circuit potential (OCP), which correspond to oxidized DMPO (A_N = 15.0 G), and another four peaks appear when gradually charging to 0.8 V (denoted as C-0.8 V). The simulation result indicates that the newly emerged peaks at the charging potential of 0.8 V versus SCE are assigned to typical DMPO-adduct signals (Figure 5D), ·OH with $A_{H\beta} = A_N$ = 14.8 G [50], because of the formation of *OH. The peaks associated with the formation of *OH become stronger when charging to 0.9 V (denoted as C-0.9 V) due to the increased water dissociation. These results coincide well with the in situ Raman and DFT calculations, producing strong evidence of water dissociation. Moreover, the theoretical calculation and simulation (Figure S34) exclude the two-electron transfer reaction (*O) and three-electron transfer reaction (*OOH), indicating the absence of further electron transfer after the water dissociation. In comparison, no obvious DMPO-·OH signal can be observed on the MnO_2 electrode even at 0.9 V versus SCE, as shown at the bottom of Figure 5C. To examine the reversibility of water dissociation on the DV-MnO_2, ex situ EPR tests were conducted during discharging (Figure 5E), where the signal associated with ·OH disappears at 0.7 V versus SCE. The ·OH quenching experiment shows the reduction of ·OH at 0.77 V versus SCE (Figure S35), slightly higher than that of in situ Raman results due to strong binding of *OH species with DV-MnO_2.

To observe the spin evolution of the electrode materials, in situ EPR measurements were also carried out in water without Na_2SO_4. The weak EPR signal at approximately 1500 G is assigned to the Fe^{3+} from the capillary (Figure S36). The signals for the MnO_2 at different potentials remain almost unchanged (Figure 5F). Nevertheless, the signals of the DV-MnO_2 remain unchanged in the potential range from 0 to 0.7 V versus SCE (left panel of Figure 5G), but intensify and narrow from 0.7 to 0.9 V versus SCE (right panel of Figure 5G). Such a variation is due to the decrease of electron-electron dipolar interaction as discussed above, suggesting the consumption of delocalized e_g electron to facilitate water dissociation. Based on the aforementioned observation, the polarization could be attributed to water dissociation, which is the origin of the extra pseudocapacitive energy for DV-MnO_2.

To quantify the extra specific capacitance provided by water dissociation, electrochemical tests were performed in a non-aqueous tetraglyme-based electrolyte, where only Na^+ ions participate in the energy storage and exclude contributions from H_2O (including H_2O insertion/extraction and water dissociation). Furthermore, the large molecular size of tetraglyme renders its intercalation pseudocapacitance into the MnO_2 interlayers negligible. As shown in Figure S37, both electrodes display similar CV shapes. Comparing CV curves in the two electrolytes, the specific capacitance can be divided into several parts as shown in Figure S37c. The intrinsic redox pseudocapacitance (192.1 F g^{-1}) of the MnO_2 electrode, with an additional 6.4 F g^{-1} in the aqueous electrolyte attributed to the H_2O insertion [47]. For the DV-MnO_2 electrode, the specific capacitance in the tetraglyme-based electrolyte is 212.4 F·g^{-1}, consisting of 192.1 F·g^{-1} from intrinsic redox pseudocapacitance and

20.3 $F \cdot g^{-1}$ from defect sites. In the aqueous electrolyte, the specific capacitance is higher by 38.06 $F \cdot g^{-1}$, which includes 6.4 $F \cdot g^{-1}$ from water intercalation and 31.66 $F \cdot g^{-1}$ from the water dissociation process. Therefore, at a scan rate of 2 $mV \cdot s^{-1}$, the single-electron dissociation process of water molecules provides approximately 12.6% extra pseudocapacitance.

Given that defect-rich MnO_2 contains a high proportion of low-valence manganese ions and water dissociation with *OH intermediate formation on the electrode surface, the Jahn–Teller effect is likely to occur during electrochemical cycling, potentially leading to active material detachment and consequent degradation of electrochemical performance. To evaluate the electrochemical stability, long-term cycling tests were conducted on the DV-MnO_2 electrode, as shown in Figure **S38**. During the first 600 cycles, the specific capacitance gradually increases owing to electrochemical activation, after which it stabilizes at approximately 160 $F \cdot g^{-1}$. Throughout the cycling process, the Coulombic efficiency remains consistently above 98%, indicating a stable and highly reversible electrochemical reaction. As shown in Figure **S39**, the post-cycling SEM images reveal that the DV-MnO_2 electrode retains a uniform nanoflower morphology. The valence state distribution of Mn ions, as probed by Mn 2*p* XPS, exhibits no significant difference between the cycled electrode (Figure **S40**) and the fresh one. Moreover, the manganese ion concentration in the cycled electrolyte is approximately 15 $\mu g \cdot L^{-1}$ (Table **S2**), suggesting minimal dissolution of MnO_2. Additionally, the polarization peak at high potentials is still discernible in the CV curve after cycling, confirming the stability of the single-electron water dissociation reaction (Figure **S41**).

3 Conclusion

In summary, a novel structure that can utilize the side reaction of water dissociation for extra pseudocapacitive energy storage has been theoretically proposed and successfully fabricated. Theoretical calculations indicate that MnO_2 with Mn and O vacancies, featuring e_g electron filling, allows reversible water dissociation through the Mn^{3+} (e_g^1)–O^{2-}–Mn^{4+} (t_{2g}^3) double exchange channel. Subsequently, DV-MnO_2 was successfully prepared by extracting Mn and O from MnO_2 using a strong chelating agent, LEDA. Compared to MnO_2, a 53% increase in capacitance was observed for DV-MnO_2. The origin of the additional capacitance has been attributed to reversible water dissociation, as confirmed by in situ Raman and self-developed in situ EPR. This work not only deepens our understanding of aqueous-based energy storage mechanisms but also provides theoretical insights for manipulating the spin state of transition metal oxides for electrochemical energy storage applications.

Author Contributions

Y.W., A.J.F., and H.H. performed conceptualization. Y.W., B.W., D.L.Z., Q.L., A.J.F., M.B.W., and H.H. performed methodology. Y.W. performed theoretical calculations. Y.W., Y.J.X., and T.C. performed investigation. Y.W. and Y.J.X. performed visualization. H.H. performed supervision. Y.W. and H.H. wrote the original draft. Y.W., B.W., A.J.F., and H.H. wrote the review and editing.

Acknowledgements

This work was financially supported by Qingdao Natural Science Foundation (24-8-4-zrjj-5-jch), Shandong Provincial Natural Science Foundation (ZR2023LFG005), the Key Research and Development Program of Shandong Province (2024ZLGX08), Shandong Provincial Excellent Young Scientists Fund Program (Overseas) (2024HWYQ-047), Taishan Scholars Program of Shandong Province (tsqn20221117), Innovation fund project for graduate student of China University of Petroleum (East China) and the Fundamental Research Funds for the Central Universities (No. 24CX04023A).

Conflicts of Interest

The authors declare no conflicts of interest.

Data Availability Statement

The data that support the findings of this study are available in the supplementary material of this article.